NUMERICAL SIMULATIONS OF TWO-WAY COUPLED MAGNETIC DYNAMOS IN COMPLEX GEOMETRIES

Saša Kenjereš and Kemal Hanjalić*
Department of Multi Scale Physics, Faculty of Applied Sciences
and J. M. Burgerscentre for Fluid Dynamics,
Deft University of Technology,
Lorentzweg 1, 2628 CJ Delft, The Netherlands
S.Kenjeres@TUDelft.nl

ABSTRACT

We report on hybrid numerical simulations of a turbulent magnetic dynamo. The simulated setup mimics the Riga dynamo experiment characterized by hydrodynamic Reynolds $Re \approx 3.5 \times 10^6$ and magnetic Reynolds number $15 \leq Re_m \leq 20$, Gailitis *et al.* (2000). The simulations were performed by simultaneous fully coupled solution of the transient Reynolds-Averaged Navier-Stokes (T-RANS) equations for the fluid velocity and turbulence field, and the direct numerical solution of the magnetic induction equations (DNS). This fully integrated hybrid T-RANS/DNS approach, applied in the finite-volume numerical framework with a multi-block-structured non-orthogonal geometry-fitted computational mesh, reproduced the mechanism of self-generation of a magnetic field in close accordance with the experimental records. In addition to the numerical confirmation of the Riga findings, the numerical simulations provided detailed insights into the temporal and spatial dynamics of flow, turbulence and electromagnetic fields and their reorganization due to mutual interactions, revealing the full four-dimensional picture of a dynamo action in the turbulent regime under realistic working conditions.

INTRODUCTION

A magnetic dynamo is a process of conversion of the mechanical energy of a moving electrically conductive medium into the magnetic energy. It is believed that the magnetic dynamo effects are responsible for creation and for sustenance of magnetic fields in spiral galaxies, stars and planets (including Earth magnetic field). In addition to these fundamental physical phenomena at huge scales, interactions between fluid flow, turbulence and electromagnetic fields play the key role in many technological applications. Examples include: electromagnetic breaking in continuous casting of steel, semiconductors crystal growth, arc-welding, electromagnetic mixing and steering in metallurgical process, liquid metal blankets of fusion reactors (tokamak), etc.

The experimental studies of magnetic dynamos face many practical problems and limitations associated with large dimensions of set-ups and potentially dangerous working fluids (such as liquid sodium). This explains why, despite a lot of effort, the first ever experimental proof of a dynamo action was reported only in late 1999 when the two experimental groups, in Riga (Gailitis *et al.*, 2000, 2001, 2002) and Karlsruhe (Stieglitz and Müller, 2001, 2002), independently observed self-excitation and the subsequent sustenance of the magnetic field. Despite their undisputed success, these experimental studies provided only the time records of the magnetic field components at particular locations - so information addressing the detailed time and spatial distribution of the magnetic field and its dynamics are still missing.

At present, the only way to provide detailed three-dimensional information on complex physics of time-dependent fluid flow, turbulence and electromagnetic field interactions is numerical simulation. Of course, before exploiting the numerical results to gain a deeper physical insights into specific phenomena, the computer simulations must be verified and proven to be numerically accurate and the mathematical models used to close the equation set to be based on solid physical foundation.

In this study, we propose a hybrid approach involving simultaneous solving of the two-way coupled fluid flow and electromagnetic interactions. For the fluid flow variables (velocity, pressure and turbulence) we introduce the transient Reynolds-Averaged Navier-Stokes (T-RANS) method, whereas a fully resolving (DNS) approach was used for the electromagnetic variables. The justification of a such an approach is motivated by a huge disparity of characteristic length and time scales for velocity and electromagnetic fields, respectively. For working conditions of the Riga dynamo setup it can be estimated that the typical magnetic diffusive length scale, defined as $\eta_B = \left(\lambda^3/\varepsilon\right)^{1/4}$, is much larger than the typical viscous (Kolmogorov) velocity scale, $\eta_u = \left(\nu^3/\varepsilon\right)^{1/4}$ since the magnetic Prandtl number estimated from the liquid sodium properties gives $Pr_m = \nu/\lambda = (\eta_u/\eta_B)^{4/3} \approx 6.5 \times 10^{-6}$.

In order to mimic the realistic experimental conditions, the fully-developed steady RANS solutions were performed first. In this stage, the magnetic induction equations were not solved. If the velocity fields and turbulence levels are properly captured, such calculated fields will represent a proper basis for possible capturing of the self-generation of a magnetic field when critical parameters (saturation levels) are reached. When fully convergent solutions were obtained, the magnetic induction equations is activated. For each time step a series of iterations are performed until the convergent fields are finally obtained. In contrast to the previous segregated numerical simulations, this iterative procedure involves simultaneous solution of both the momentum and magnetic induction equations with implicitly updated (the most recent) fields. This procedure is advanced in time reproducing the growth of a self-generated magnetic field. The generated magnetic field creates the Lorentz force, which feeds back into the momentum equation and, ultimately, the saturation magnetic regime is achieved.

*Present affiliation: Marie Curie Chair, Department of Mechanics and Aeronautics, University of Rome 'La Sapienza', Italy.

EQUATIONS AND SUBSCALE MODEL OF TURBULENCE

The governing fluid momentum and magnetic induction equations that describe the two-way coupled fluid flow/electromagnetic interactions can be written as:

$$\frac{\partial \hat{U}_i}{\partial t} = \frac{\partial}{\partial x_j}\left[\nu\left(\frac{\partial \hat{U}_i}{\partial x_j} + \frac{\partial \hat{U}_j}{\partial x_i}\right) - \hat{U}_i\hat{U}_j\right] - \frac{1}{\rho}\frac{\partial \hat{p}}{\partial x_i} + \underbrace{\frac{1}{\rho\mu_0}\left(\hat{B}_j\frac{\partial \hat{B}_i}{\partial x_j} - \hat{B}_j\frac{\partial \hat{B}_j}{\partial x_i}\right)}_{\mathbf{F^L} = \hat{\mathbf{J}}\times\hat{\mathbf{B}} = \mathbf{1}/\mu_0\left(\nabla\times\hat{\mathbf{B}}\right)\times\hat{\mathbf{B}}} \quad (1)$$

$$\frac{\partial \hat{B}_i}{\partial t} = \frac{\partial}{\partial x_j}\left(\frac{1}{\mu_0\sigma}\frac{\partial \hat{B}_i}{\partial x_j} - \hat{B}_i\hat{U}_j + \hat{U}_i\hat{B}_j\right) \quad (2)$$

The equation set is closed with the divergency free conditions $\partial\hat{U}_j/\partial x_j$=0, $\partial\hat{B}_j/\partial x_j$=0 for the velocity and magnetic fields, respectively. It can be seen that these equations are directly interconnected through the Lorentz force in the momentum equation and the convective term in the magnetic induction equation. Since the fully resolving approach will be applied for the magnetic induction, the original form of this equations for the three coordinate directions are discretised. For the momentum equations, in order to obtain the evolution equations for the ensemble-mean variables, the Reynolds decomposition is introduced. All instantaneous variables are represented as a sum of the ensemble averaged and fluctuating contributions, i.e. $\hat{U}_i = \langle U_i\rangle + u_i^{'} = U_i + u_i$, $\hat{P} = \langle P\rangle + p^{'} = P + p$, $\hat{B}_i = \langle B_i\rangle + b_i^{'} = B_i + b_i$, etc. The ensemble-averaged momentum equations can then be written as:

$$\frac{\partial U_i}{\partial t} = \frac{\partial}{\partial x_j}\left[\nu\left(\frac{\partial U_i}{\partial x_j} + \frac{\partial U_j}{\partial x_i}\right) - U_iU_j - \left(\tau_{ij}^u - \tau_{ij}^b\right)\right] - \frac{1}{\rho}\frac{\partial P}{\partial x_i} + \frac{1}{\rho\mu_0}\left(B_j\frac{\partial B_i}{\partial x_j} - B_j\frac{\partial B_j}{\partial x_i}\right) \quad (3)$$

where $\tau_{ij}^u = \langle u_iu_j\rangle$, $\tau_{ij}^b = 1/\rho\mu_0\langle b_ib_j\rangle$ are the ensemble averaged second moments of the velocity and magnetic field fluctuations, respectively. In order to close the system of the ensemble-averaged equations, additional relations (turbulence closure models) are needed to account for the subscale turbulence contributions. The most natural way to obtain these correlations is to derive the full transport equations for $\langle u_iu_j\rangle$, $\langle b_ib_j\rangle$, $\langle u_ib_j\rangle$ etc. Such a system of equations becomes very complex with many terms that should again be approximated (modeled) involving even higher order correlations (triple moments, correlations involving fluctuating pressure, derivatives of the fluctuating velocity and magnetic field, and others). The difficulty is not only in the sheer number of equations but also in our present inability to model and to evaluate such correlations since that process requires simultaneous measurement of the fluctuating velocity and electromagnetic fields. Such details can only be extracted from DNS. Unfortunately, at present, such DNS studies of the induction and the dynamo action at low Pr_m are still in rudimentary phase and oriented primarily towards providing magnetic and kinematic spectra, Ponty *et al.* (2004), Ponty *et al.* (2005), Mininni *et al.* (2005).

In our previous works we developed RANS models at different levels - including a full-second moment closure (Kenjereš *et al.* (2004) and a simplified eddy-viscosity based model (Kenjereš and Hanjalić (2000), for turbulent flows subjected to an external magnetic field. These closures are developed for the subscale τ_{ij}^u turbulent stresses. In the second-moment closure, the full transport equations for all components of the turbulent stress are solved. This enables the capturing of the mechanism of the fluctuation distributions among the particular velocity components so that the effects of turbulence anisotropy can be properly modeled. The turbulence anisotropy is of crucial importance for accurate predictions for flows in proximity of solid walls and when subjected to external body forces. For the Riga dynamo experimental setup with a strongly turbulent helical motion in the inner cylinder (high Reynolds number), the near-wall effects are of the secondary importance. Additionally, since it is our first attempt to perform fully two-way coupled magnetic dynamo simulations in realistic working conditions (geometry, flow, turbulence and electromagnetic parameters), we will proceed with a simplified eddy viscosity model. Now, instead of solving the full set of the second-moment equations, the transport equations for the turbulence kinetic energy ($\langle k\rangle = 0.5\langle u_iu_i\rangle$) and its dissipation rate ($\langle\varepsilon\rangle = 2\nu\langle(\partial u_i/\partial x_j)^2\rangle$) are solved:

Table 1: Specification of the model coefficients.

$C_{\varepsilon 1}$	$C_{\varepsilon 2}$	C_L	σ_k	σ_ε	C_μ
1.44	1.92	0.025	1.	1.3	0.09

$$\frac{\partial\langle k\rangle}{\partial t} = \frac{\partial}{\partial x_j}\left(\nu\frac{\partial\langle k\rangle}{\partial x_j} + \mathcal{D}_k^t - \langle U_j\rangle\langle k\rangle\right) - \tau_{ij}^u\frac{\partial\langle U_i\rangle}{\partial x_j} - \langle\varepsilon\rangle - P_k^b \quad (4)$$

$$\frac{\partial\langle\varepsilon\rangle}{\partial t} = \frac{\partial}{\partial x_j}\left(\nu\frac{\partial\langle\varepsilon\rangle}{\partial x_j} + \mathcal{D}_\varepsilon^t - \langle U_j\rangle\langle\varepsilon\rangle\right) - C_{\varepsilon 1}\tau_{ij}^u\frac{\partial\langle U_i\rangle}{\partial x_j}\frac{\langle\varepsilon\rangle}{\langle k\rangle} - C_{\varepsilon 2}\frac{\langle\varepsilon\rangle^2}{\langle k\rangle} - P_\varepsilon^b \quad (5)$$

where

$$\mathcal{D}_k^t = -\frac{1}{\rho}\langle u_ip\rangle - \langle u_jk\rangle = \frac{\nu_t}{\sigma_k}\frac{\partial\langle k\rangle}{\partial x_j},$$
$$\mathcal{D}_\varepsilon^t = -2\frac{\nu}{\rho}\langle\frac{\partial p}{\partial x_k}\frac{\partial u_j}{\partial x_k}\rangle - \nu\langle u_j\left(\frac{\partial u_i}{\partial x_k}\right)^2\rangle = \frac{\nu_t}{\sigma_\varepsilon}\frac{\partial\langle\varepsilon\rangle}{\partial x_j}$$
$$P_k^b = \frac{\sigma}{\rho}B_0^2\langle k\rangle exp\left(-C_L\frac{\sigma}{\rho}B_0^2\frac{\langle k\rangle}{\langle\varepsilon\rangle}\right),\ P_\varepsilon^b = P_k^b\frac{\langle\varepsilon\rangle}{\langle k\rangle} \quad (6)$$

are turbulent diffusion ($\mathcal{D}_k^t, \mathcal{D}_\varepsilon^t$) modeled by a simple gradient diffusion hypothesis, whereas the 'magnetic' production/destruction terms (P_k^b, P_ε^b) are modeled by introducing the locally determined turbulence parameters and the time scale of the magnetic damping (Kenjereš and Hanjalić, 2000), respectively. Here $B_0 = \sqrt{B_i^2}$ is the intensity of the magnetic field. The kinematic turbulent stresses are then evaluated as:

$$\tau_{ij}^u = \frac{2}{3}\langle k\rangle\delta_{ij} - \nu_t\left(\frac{\partial\langle U_i\rangle}{\partial x_j} + \frac{\partial\langle U_j\rangle}{\partial x_i}\right),\ \nu_t = C_\mu\frac{\langle k\rangle^2}{\langle\varepsilon\rangle} \quad (7)$$

The complete specification of the model coefficients is given in Table 1. Note that with this model, both the direct (through the momentum equations) and the indirect (through the MHD terms in the turbulence equations, P_k^b, P_ε^b), the effects of the Lorentz force onto the fluid flow and turbulence are introduced. This model was extensively validated in a series of generic situations including fully developed turbulent channel flows (Kenjereš *et al.*, 2004;

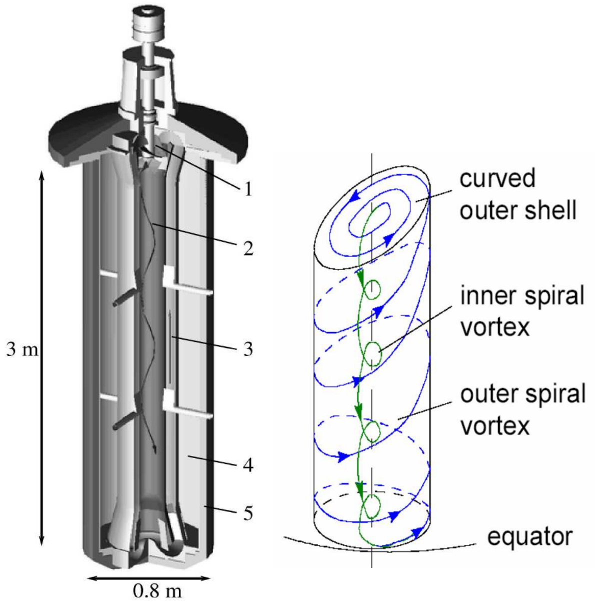

Figure 1: Right- sketch of the columnar vortex pattern of convection inside of Earth according to Busse (2000); Left- Riga dynamo experimental setup, Gailitis *et al.* (2000,2001,2002): 1-propeller, 2-inner cylinder with helical flow, 3-outer passage with back flow, 4-surrounding ring of sodium at rest, 5-thermal insulation.

Kenjereš and Hanjalić, 2000), turbulent thermal convection in enclosures (Kenjereš and Hanjalić, 2004) unsteady electromagnetically driven recirculating melt flows (Schwarze and Obermeier, 2004) and control of the crossing-shock turbulent layer in magnetogasdynamic applications (Gaitonde and Miller, 2005). For all the above mentioned applications, the fluid flow was subjected entirely or locally to external magnetic fields of different orientations and strength, i.e. a wide range of flow regimes (weakly or highly turbulent flows with or without heat transfer), and intensities of electromagnetic interactions (weak or strong interactions) are simulated. This variety of different flow situations and applications give reasonable confidence in the validity of the above introduced model for simulating turbulent flows subjected to the Lorentz force. The remaining magnetic turbulent stress τ_{ij}^{b} is negligible for the particular Riga dynamo setup.

SPECIFICATION OF BOUNDARY CONDITIONS

The boundary conditions for all fluid flow and turbulence parameters along the solid walls are imposed through the set of wall-functions. This is the only viable alternative for high Reynolds number flows in complex domains because a full numerical resolving of boundary layers along the solid walls at such high Re numbers would require modification of all equations for the viscous and non-viscous wall effects and the application of a much finer computational grid, which would require very large computational effort. We note, however, that the viscous wall effects play secondary role in the Riga dynamo setup since the highly turbulent swirling flow pattern inside the inner cylinder determines to a large degree the flow features in the whole rig. Nevertheless, in order to properly capture the high gradients of velocity in the near-wall regions, the numerical mesh is always clustered in these regions. The numerical mesh is so designed to ensure that the first near-wall grid point is always located at the nondimensional distance (normalized with the inner-wall scales) in the range $40 \leq r^+(x^+, z^+) \leq 100$. Instead of simulating the flow through the rotating propeller, for which a complex moving mesh would be needed, we mimic the propeller by imposing both the axial and tangential velocity projections in the inner cylinder at the propeller exit plane. These values are kept constant during the entire simulation. Since the direct velocity measurements for the realistic working conditions are not available, we scaled-up velocity components measured in the 1:2 scale-down water model of the Riga dynamo setup, Gailitis *et al.* (2000,2001).

In contrast to momentum and turbulence parameters equations, the magnetic induction equation is solved in the inner and outer cylinders, in the dividing walls and in the surrounding ring of the sodium at rest. Additional difficulty appeared in the specification of the non-local boundary conditions for the electromagnetic variables. In the previous work of Gailitis *et al.* (2004), where the two-dimensional finite-difference based kinematic solver was tested for a simplified Riga dynamo setup, the Laplace equation was solved in the vacuum exterior and matching conditions are imposed at the outer walls of the surrounding ring of sodium at rest. Such an approach for three-dimensional geometries reduce significantly the numerical effectiveness of the solver. This is the main reason why we followed here a simplified approach by which we imposed the vertical magnetic field boundary condition at the outer wall of the surrounding ring of sodium at rest in accordance with Brandenburg *et al.* (1995) and Hamba (2004). This boundary condition allows an escape of the self-generated magnetic field from the discretised domain while still keeping reasonable critical dynamo thresholds (a difference of 20% between the theoretically determined and numerically estimated critical thresholds in the Riga dynamo setup, Gailitis *et al.* (2004).

In this study we performed additional extensive validation of this boundary condition in the kinematic mode (without back-reaction of the self-generated magnetic field on the fluid flow) and proved that the critical dynamo threshold is reached for $Re_m > 15$. This value is in good agreement with the theoretically estimated critical threshold of $Re_m^c = 17.7$, based on studies of the convective instabilities of the Ponomarenko dynamo, Gailitis *et al.* (2002,2004). In the work of Avalos-Zuniga *et al.* (2003) an assessment of different electromagnetic boundary conditions on the onset of a magnetic dynamo action is performed. Both the Riga dynamo and the Karlsruhe-dynamo experimental setups were analyses in details. It was concluded that an inclusion of a stagnant surrounding layer always resulted in reducing the critical threshold, what appeared to be very convenient from the practical point of view for the realization of a magnetic field self-excitation. Obviously, as long as this layer is included in the numerical simulations, simplified boundary conditions for electromagnetic variables (the vertical field conditions) will be a reasonable first approximation. Finally, it is concluded that for the first series of fully-coupled two-way simulations targeting numerical reproduction of the self-generation of a magnetic field in the Riga dynamo setup, the vertical magnetic field condition was found sufficient.

THE FINITE-VOLUME DISCRETIZATION OF EQUATIONS

The finite-volume approach, used here for the simultaneous solving of fluid flow, turbulence and electromagnetic fields, is based on the pre-integration of the field equations over an elementary control volume, thus ensuring the conservation of all variables over each grid cell. All transport variables are located in the geometrical center of such

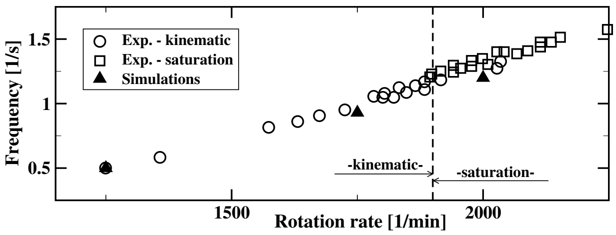

Figure 2: The self-induced magnetic field frequency in function of the rotation rates in the Riga dynamo setup for kinematic (one-way) and saturation (two-way coupled) regimes. Experimental data from Gailitis *et al.* (2004).

control volumes (collocated variable arrangement). The Cartesian vector and tensor components are used for representing a general non-orthogonal numerical mesh. The grid-nonorthogonality is included through the local curvilinear coordinate system (x^j) with the Jacobian (J) and β_m^j representing the cofactor of $\partial x_i/\partial x^j$ coordinate transformation, $\frac{\partial}{\partial x_i} \approx \frac{1}{J}\frac{\partial}{\partial x^j}\left(\dots\, \beta_m^j\right)$. This, together with the fact that the product $J{\cdot}\Delta x^1{\cdot}\Delta x^2{\cdot}\Delta x^3$ represents the exact total volume (ΔV) of the control cell around the central position (P), makes that all these coordinate transformation can be easily represented in the Cartesian coordinate system. In order to prevent a decoupling between the velocity and pressure fields (checkerboard pressure oscillations) the Rhie-Chow interpolation is used in the pressure-correction equation. The corrected velocity and pressure fields are iteratively calculated by the Semi-Implicit Method for Pressure-Linked Equations (SIMPLE) algorithm. The numerical accuracy of the entire discretised system is of the second-order. The time integration is performed by the fully implicit second-order scheme based on three consecutive time steps. The diffusive terms are discretised by the second-order central differencing scheme. The remaining convective terms are calculated by the monotonicity preserving total variation diminishing scheme with the UMIST limiter. The linearized system of equations is then solved using Stone's strongly implicit procedure (SIP) based on an incomplete LU-factorization.

RESULTS AND DISCUSSION OF NUMERICAL SIMULATIONS

The results of numerically obtained frequencies of the axial magnetic field as a function of the propeller rotation rates, presented in Fig. 2, show good agreement with the experimental record. In the kinematic regime there is no back-reaction of the self-generated magnetic field onto the fluid flow, and an exponential growth or decay of the seed magnetic field takes place. After this initial growth of the self-generated magnetic field in the kinematic regime, the Lorentz force grows and soon becomes strong enough to significantly affect the underlying fluid flow and turbulence. Since an increase in the Lorentz force imposes a stronger braking of fluid motion, it essentially reduces the source of self-generation of the magnetic field. Eventually, in the saturation regime a balance is reached, characterized by a zero-growth rate of magnetic field intensity.

The radial profiles of the self-generated magnetic field components are shown in Fig. 3. Here, the symbols represent the experimentally recorded maximum values at the particular radial locations for different propeller rotation rates - ranging from 1900 to 2500 rpm, Gailitis *et al.* (2006). All profiles are rescaled with the maximum value along the radial direction. It can be seen that for both the axial and

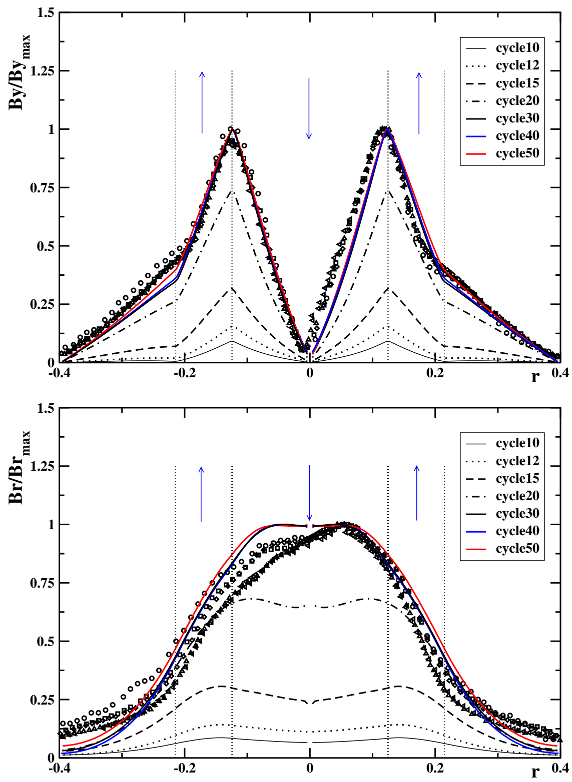

Figure 3: Radial dependency of the non-dimensional magnetic field distributions, Above: axial; below: radial component. The symbols represent experimental values obtained at different rotational rates of the propeller, ranging from 1900 to 2500 rpm. The lines represent numerically obtained values for different time instants.

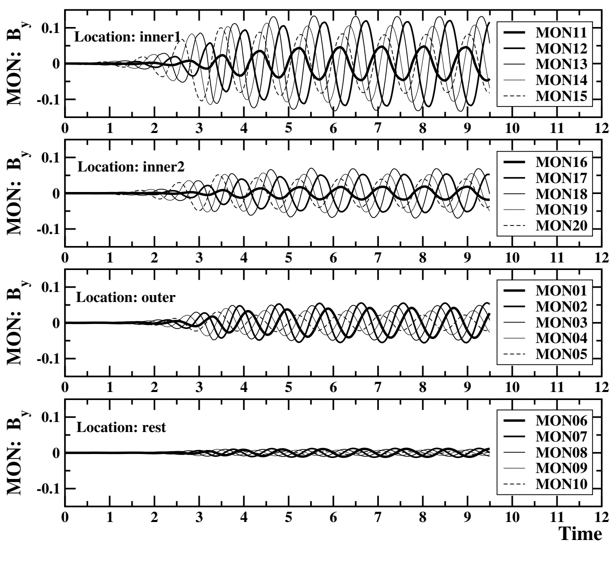

Figure 4: Time evolution of the axial magnetic field component (B_y) at the characteristic locations distributed along vertical lines in the inner cylinder (inner1 and inner2), outer passage (outer) and surrounding ring of sodium (rest), respectively.

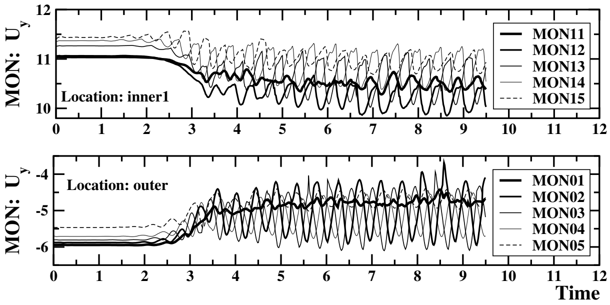

Figure 5: Time evolutions of axial velocity components (U_y) at particular monitoring locations.

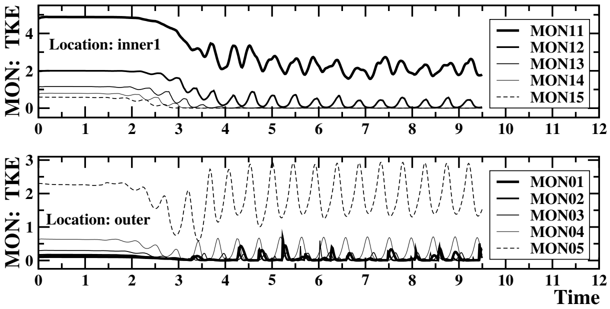

Figure 6: Time evolutions of the turbulent kinetic energy ($TKE{=}\langle k\rangle{=}0.5\overline{u_i^2}$ in $[m^2/s^2]$) at monitoring locations.

radial magnetic field component, experiments show a slight deviation in profiles symmetry. In contrast, the numerical results show perfect symmetry indicating full convergence of the magnetic induction equation. It can be seen that very good agreement between the experimental and numerical recordings is achieved for the axial magnetic field component, Fig. 3-above. The results for the radial magnetic field component show a larger scatter, but again, agreement can be considered as good, Fig. 3-below. In contrast to the zero axial magnetic field at the outer boundary of the surrounding sodium at rest, the radial component correctly shows a final value. This boundary peak value is slightly underpredicted as compared with measurements, but shows clearly that the boundary conditions for the vertical magnetic field is properly imposed. In contrast to the monotonic time evolution of the axial magnetic field profiles, the radial profiles show an interesting variation in the radial location of the peak value. The peak value travels from the center of the outer cylinder for earlier time instants (cycle10-cycle15) and finally settles at the middle radial distance in the inner cylinder, Fig. 3-below.

The entire time-series of the axial magnetic field self-generation are shown in Fig. 4. Here the monitoring points are distributed along the vertical lines that are located at different positions. The evolutions show the highest levels of amplification in the middle part of the setup ($MON13$). In addition to this vertical dependency, a strong radial variation of the recorded signals is clearly visible with the strongest amplification in proximity of the wall dividing the inner from the outer cylinder.

A similar oscillatory behavior is observed for the axial velocity profiles, Fig. 5. Starting from the statistically steady and convergent solutions, as the self-generated magnetic field grows, the Lorentz force increases and begins to influence the underlying fluid flow. In the fully saturated regime (for time instants > 3 sec) periods with intensive disturbances are observed. Such oscillatory behavior of the velocity field

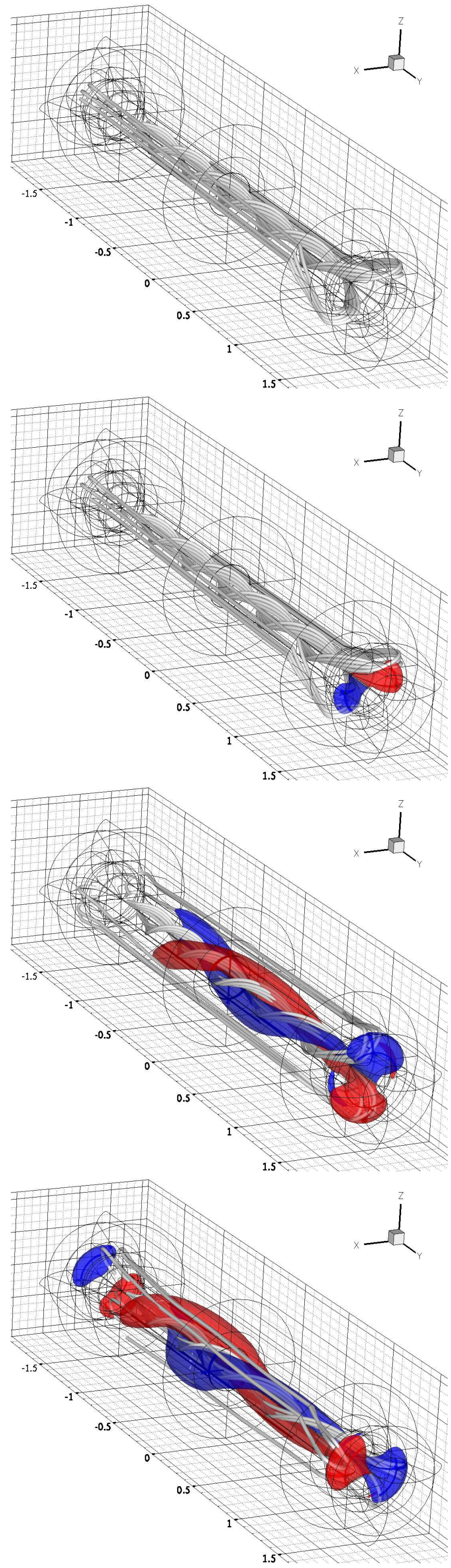

Figure 7: Time evolution of the radial magnetic field (B_r = 0.015 (red), −0.015 (blue) in $[T]$) with streak-lines (gray tubes): cyle10, cycle12, cycle20, cycle40, respectively.

illustrates that fully coupled two-way interactions between the fluid flow and electromagnetic field are simulated. It is interesting to note the selective response of the turbulent kinetic energy in the inner and outer cylinder, Fig. 6. While the turbulent kinetic energy is highly suppressed in the inner cylinder at all locations (Fig. 6-above), it is significantly enhanced in the outer cylinder (Fig. 6-below).

In contrast to measurements, the numerical simulations can provide full three-dimensional spatial distributions of the self-generated magnetic field. In Fig. 7 the isosurfaces of axial magnetic field of an opposite sign (red and blue) are shown together with stream-traces of the instantaneous velocity field (gray tubes). The strongest self-amplification takes place in the lower part of the setup and then it moves upwards. This vertical upward shift is also observed in the experiments and explained in terms of a simultaneous reduction of both the axial and tangential velocity components in the lower part of the inner cylinder, as shown in Fig. 7. Animations reveal a pattern of slowly rotating asymmetric magnetic field, with a frequency of approximately 1 Hz. This is significantly different from the typical frequency of the propeller that is approximately 30 Hz.

CONCLUSIONS

The paper reports on two-way-coupled hybrid numerical simulations of the full-scale Riga dynamo experiment, in which the experimental configuration, fluid properties and externally imposed parameters have all been closely replicated, reproducing thus realistic working conditions with Re=3.5 × 10^6, Re_m=18. The simulations are performed by solving the time-dependent ("transient") transport equations for the ensemble averaged fluid flow and turbulence variables (T-RANS) simultaneously with the direct numerical solutions of the magnetic induction equations (DNS). The T-RANS equations have been closed using an earlier developed eddy-viscosity model for the subscale turbulence contributions in which the effects of the fluctuating Lorentz force have been included. The fluid-flow and electromagnetic equations are solved using a fully integrated finite-volume Navier-Stokes/Maxwell solver for three-dimensional non-orthogonal geometries.

The fully coupled (two-way) simulations reproduced closely the experimentally recorded self-excitation and the subsequent saturated self-sustenance of the generated magnetic field. Detailed comparisons revealed that the simulated features of the self-excitation and sustenance, including frequencies, amplitudes and spatial distributions of magnetic fields are all in good agreement with the available experimental data. In addition to the numerical verification of the experimental main findings - the histogram of the magnetic field self-excitation, saturation and self-sustenance, the simulations provided data on full time and space dynamics of the fluid velocity, turbulence statistics and magnetic field, from which practically any information and deductions could be extracted - of course within the framework of the ensemble-averaged time dynamics.

ACKNOWLEDGMENTS

The results reported in this paper emerged from the research project "MAGDYN: Magnetic Field Dynamos - Laboratory Studies based on the Riga Dynamo Facility", sponsored by the European Commission contract HPRI-CT-2001-50027. In the framework of this research project, Dr. F. Stefani, Dr. G. Gerbeth and Prof. A. Gailitis are gratefully acknowledged for numerous discussions and for providing the experimental data. Mr. S. Renaudier is acknowledged for his involvement in generation of the numerical grid. The research of Dr. S. Kenjereš has been possible by a fellowship of the Royal Netherlands Academy of Arts and Sciences (KNAW). The supercomputing facilities have been provided by the National Computing Facilities Foundation (NCF) and sponsored by the Netherlands Organization for Scientific Research (NWO).

REFERENCES

Avalos-Zuniga R., Plunian F. and Gailitis A., 2003, *Physical Review E* **68**(6), 066307.

Brandenburg A. *et al.*, 1995, *The Astrophysical Journal* **446**, 741-754

Busse F. H., 2000, *Annual Review of Fluid Mechanics* **32**, pp.383-408.

Gailitis A. *et al.*, 2000, *Phys. Rev. Lett.* **84**, pp.4365-4368

Gailitis A. *et al.*, 2001, *Phys. Rev. Lett.* **86**, pp.3024-3027

Gailitis A. *et al.*, 2002, *Rev. Mod. Phys.* **74**, pp.973-990

Gailitis A., Lielausis O., Platacis E., Gerbeth G. and Stefani F., 2004, *Phys. Plasmas* **11**, pp.2838-2843.

Gailitis A., Lielausis O., Platacis E., Gerbeth G. and Stefani F., 2006, *Proc. 15th Riga and 6th PAMIR Conference on Fundamental and Applied MHD*, Riga, Latvia, pp.15-20.

Gaitonde D. V. and Miller J. H., 2005, *AIAA Journal* **43**(5), pp. 1064-1074.

Hamba F., 2004, *Phys. Plasmas* **11**(11), pp.5316-5327

Kenjereš S., Hanjalić K. and Bal D., 2004, *Phys. Fluids* **16**(5), pp. 1229-1241

Kenjereš S. and Hanjalić K., 2000, *Int. J. Heat and Fluid Flow* **21**(3), pp. 329-337.

Kenjereš S. and Hanjalić K., 2004, *Int. J. Heat and Fluid Flow* **25**(3), pp. 559-568.

Mininni P. D. *et al.*, 2005, *The Astrophysical Journal* **626** 853.

Ponty Y., Politano H. and Pinton J. F., 2004, *Phys. Rev. Lett* **92** 144503.

Ponty Y. *et al.*, 2005, *Phys. Rev. Lett* **94** 164502.

Schwarze R. and Obermeier F., 2004, *Modelling and Simulation in Materials Science and Engineering* **12**(5), pp. 985-993.

Stieglitz R. and Müller U., 2001, *Phys. Fluids* **13**, pp.561-564

Stieglitz R. and Müller U., 2002, *Magnetohydrodynamics* **38**, pp.27-33